Electrical Transport Properties of Large, Individual $NiCo_2O_4$ Nanoplates

Linfeng Hu, Limin Wu, Meiyong Liao, Xinhua Hu, and Xiaosheng Fang**

Understanding the electrical transport properties of individual semiconductor nanostructures is crucial to advancing their practical applications in high-performance nanodevices. Large-sized individual nanostructures with smooth surfaces are preferred because they can be easily made into nanodevices using conventional photolithography procedures rather than having to rely on costly and complex electron-beam lithography techniques. In this study, micrometer-sized $NiCo_2O_4$ nanoplates are successfully prepared from their corresponding hydroxide precursor using a quasi-topotactic transformation. The Co/Ni atomic arrangement shows no changes during the transformation from the rhombohedral LDH precursor (space group $R\bar{3}m$) to the cubic $NiCo_2O_4$ spinel (space group $Fd\bar{3}m$), and the nanoplate retains its initial morphology during the conversion process. In particular, electrical transport within an individual $NiCo_2O_4$ nanoplate is further investigated. The mechanisms of electrical conduction in the low-temperature range ($T < 100$ K) can be explained in terms of the Mott's variable-range hopping model. At high temperatures ($T > 100$ K), both the variable-range hopping and nearest-neighbor hopping mechanisms contribute to the electrical transport properties of the $NiCo_2O_4$ nanoplate. These initial results will be useful to understanding the fundamental characteristics of these nanoplates and to designing functional nanodevices from $NiCo_2O_4$ nanostructures.

1. Introduction

Low-dimensional semiconductor nanostructures have attracted significant interest in the past few years due to their unique applications in next-generation functional nanodevices, such as field-effect transistors (FETs), photodetectors, light-emitting diodes (LEDs), solar cells, and sensors.[1–4] Of particular importance to semiconductor nanostructures is electrical transport through the nanostructure. This is because predictable, controllable conductance is critical to many nanoscale electrical applications.[5–7] Therefore, study of the electrical transport properties of low-dimensional semiconductor nanostructures is crucial to promoting their practical applications in high performance nanodevices.

Cobalt-nickel oxide ($NiCo_2O_4$) is an interesting transition-metal oxide semiconductor. It is generally believed to adopt a spinel-related structure in which nickel occupies the octahedral sites and cobalt is distributed over both octahedral and tetrahedral sites.[8] In recent years, the $NiCo_2O_4$ low-dimensional nanostructure has drawn considerable attention due to its useful physical properties and wide variety of applications, most notably its electrocatalytic activity, ferromagnetic properties, and applications in the negative electrodes of lithium-ion batteries, which have been widely investigated.[9–12] Most recently, we evaluated the optoelectronic properties of $NiCo_2O_4$ nanofilm in high-frequency photodetectors.[13] The photodetector device constructed from this $NiCo_2O_4$ film showed good sensitivity and ultrafast response time of several microseconds. However, the electrical transport mechanism of $NiCo_2O_4$ nanostructures remains unclear. Generally, evaluating the conductivity of individual semiconductor nanostructures requires deposition of a pair of metal electrodes on each side of the nanostructure by a simple photolithography or a complex electron-beam lithography technique.[14,15] Larger-sized individual $NiCo_2O_4$ nanostructures are especially suitable to this means of measurement because they require individual nanostructure-device construction only using a low-cost photolithography procedure rather than a costly electron-beam lithography technique.[14] However, almost all $NiCo_2O_4$ nanostructures yet reported show poor qualities, such as a rough surface, unsatisfactory crystallinity, or very small size.[8–13,16]

Recently, it was reported that large-sized, two-dimensional (2D) layered double hydroxide (LDH) nanostructures could be prepared easily through the wet-chemical routes.[17,18] These were regarded as ideal precursors to the preparation of the corresponding oxide nanoplates.[19] In this study, inspired by previous reports, we successfully synthesized hexagonal $NiCo_2O_4$ nanoplates by thermal transformation from the corresponding CoNi-LDH precursors. We also further investigated the electrical transport properties of individual $NiCo_2O_4$ nanoplates in detail because the size and quality of the as-transformed $NiCo_2O_4$

Dr. L. F. Hu, Prof. L. M. Wu, Prof. X. H. Hu, Prof. X. S. Fang
Department of Materials Science
Fudan University
Shanghai 200433, P. R. China
E-mail: lmw@fudan.edu.cn; xshfang@fudan.edu.cn
Dr. M. Y. Liao
Optical and Electronic Materials Unit
National Institute for Materials Science (NIMS)
Namiki 1-1, Tsukuba, Ibaraki 305-0044, Japan

DOI: 10.1002/adfm.201102155

nanoplates are large and high enough for electric transport measurement from an individual nanoplate-device. Although the electrical transport properties of one-dimensional (1D) oxide nanowires have been widely reported, this is the first study of electronic transport on individual 2D oxide nanostructure.[20–24] The present work provides a new means of constructing individual 2D oxide nanostructure-based devices in an easy and inexpensive way. More importantly, the as-determined electrical properties noted in this work will be useful to the design of functional nanodevices from the $NiCo_2O_4$ nanostructures.

2. Results and Discussion

The CoNi-LDH precursor was synthesized via homogeneous precipitation as reported previously.[25] Then $NiCo_2O_4$ nanoplates were obtained by thermal transformation from the LDH precursor at an optimal condition. **Figure 1**a and d show the transmission electron microscope (TEM) morphology of the hydroxide precursor and the as-transformed $NiCo_2O_4$ nanoplate, respectively. As can be seen, the hydroxide precursor typically exhibits uniform hexagonal nanoplate morphology with a lateral size of about 3 μm and very high 2D anisotropy (Figure 1a). The nanoplate retains its initial morphology during the conversion process (Figure 1d). The selected area electron diffraction (SAED) patterns taken from individual hydroxide precursor and the as-transformed $NiCo_2O_4$ nanoplate display hexagonally arranged diffraction spots, suggesting that both hydroxide precursor and $NiCo_2O_4$ nanoplates exist as a single crystal (Figures 1b and e). The SAED patterns of the hydroxide precursor and the $NiCo_2O_4$ nanoplate can be indexed to the [001] and [111] zone axis patterns, respectively. Because the nanoplates lie flat on the copper grid perpendicular to the electron beam direction, the observed diffraction spots suggest that the top surfaces of the LDH and the $NiCo_2O_4$ nanoplates correspond to the (003) and (111) planes, respectively. This result indicates that the exposed (111) plane of the $NiCo_2O_4$ nanoplate evolved from the (003) plane of the hydroxide precursor. Further study of the crystal structure verifies that the configuration of Co/Ni atoms in the (111) plane of the $NiCo_2O_4$ crystal is similar to that of the (003) plane of the LDH crystal (as shown in Figure 1c and f). Accordingly, the Co/Ni atomic arrangement shows no changes during the transformation from the rhombohedral hydroxide precursor (space group (S.G.) $R\bar{3}m$) to the cubic $NiCo_2O_4$ spinel (S.G. $Fd\ \bar{3}m$). This means a minimal reorganization of the Co/Ni atoms in the crystal, leading to the well maintenance of hexagonal shape of the nanoplates. Due to the removal of hydroxyl groups and water molecules during the formation of the oxide crystal, this process can be called a quasi-topotactic transformation, such as has been also observed in the thermal transformations of other layered hydroxide systems.[19,26,27] It is noteworthy that the $NiCo_2O_4$ core-ring nanoplates prepared by a co-precipitation method show porous surfaces and lateral sizes less than 150 nm.[10] In contrast, the as-transformed $NiCo_2O_4$ nanoplates in the present study display smooth surfaces without any cracks, as large as several micrometers in lateral size, and superior crystallinity. Furthermore, the line-scanning elemental maps of the as-transformed $NiCo_2O_4$ nanoplate are shown in **Figure 2**, demonstrating a uniform distribution of the compositional elements Ni, Co, O inside an individual $NiCo_2O_4$ nanoplate. Therefore, these large and high-quality $NiCo_2O_4$ nanoplates may facilitate the construction of individual nanoplate devices and their subsequent electric measurement.

The UV–vis absorption spectrum of the as-transformed $NiCo_2O_4$ nanoplates is shown in **Figure 3**a. The absorption band gap energy, E_g, can be determined by the following equation:

$$(\alpha h\nu)^n = K(h\nu - E_g) \quad (1)$$

Here, $h\nu$ is the photoenergy, α is the absorption coefficient, K is a constant relative to the material, and $n = 2$ for an indirect transition and 1/2 for an allowed directed transition. The best fit gives $n = 2$, as shown in Figure 3b. The extrapolation of the straight line segment to $(\alpha h\nu)^2 = 0$ yields two absorption band gap energies of ≈2.0 eV and ≈3.3 eV. It is generally accepted that the electron configuration in the $NiCo_2O_4$ spinel structure

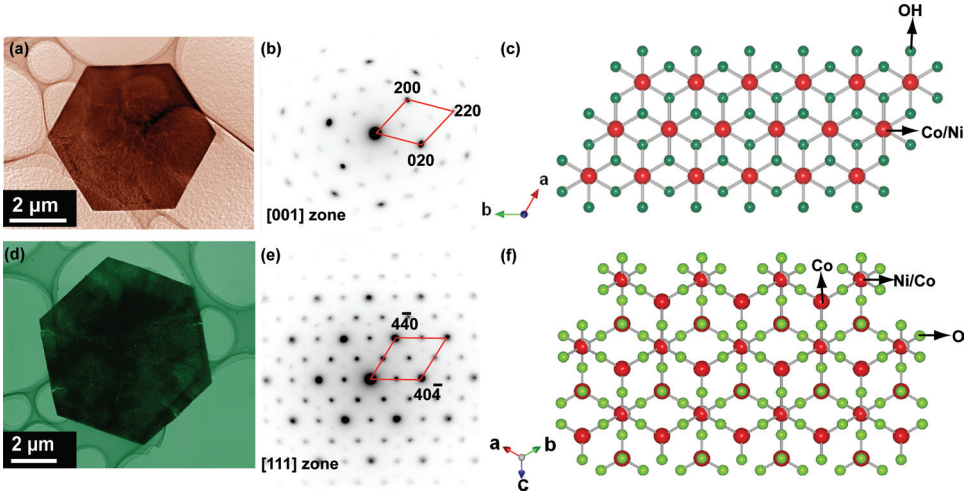

Figure 1. Typical TEM images of (a) an individual CoNi-LDH precursor nanoplate and (d) the as-transformed $NiCo_2O_4$ nanoplate. SAED patterns from (b) a single CoNi-LDH precursor nanoplate and (e) as-transformed $NiCo_2O_4$ nanoplate. Top-views of (c) CoNi-LDH (003) crystal plane and (f) $NiCo_2O_4$ (111) crystal plane.

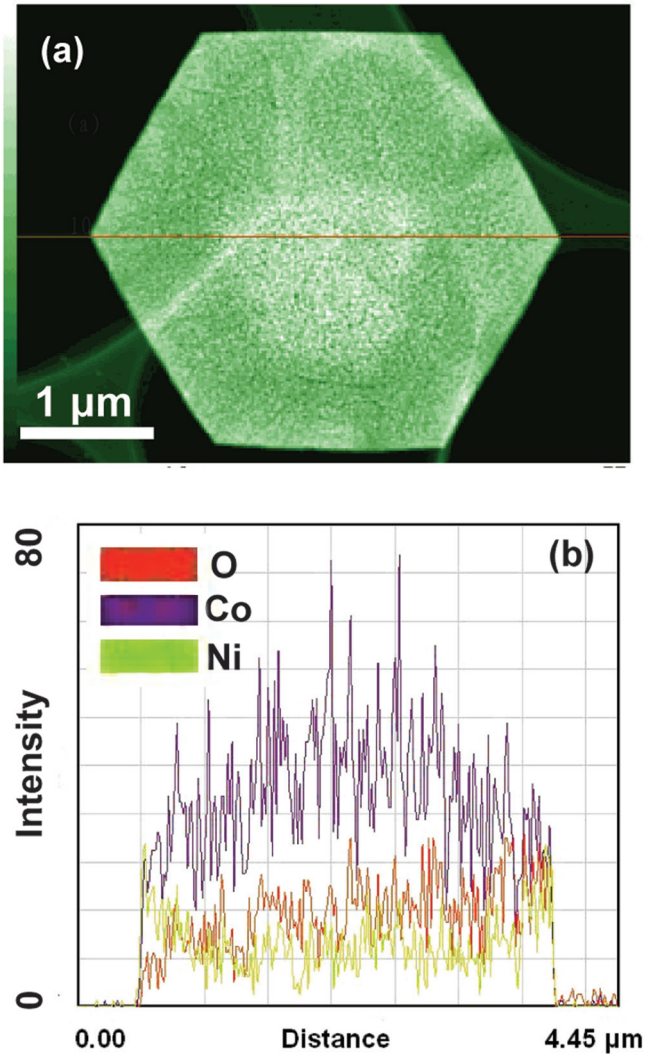

Figure 2. Line-scan profile of elemental maps across an individual $NiCo_2O_4$ nanoplate.

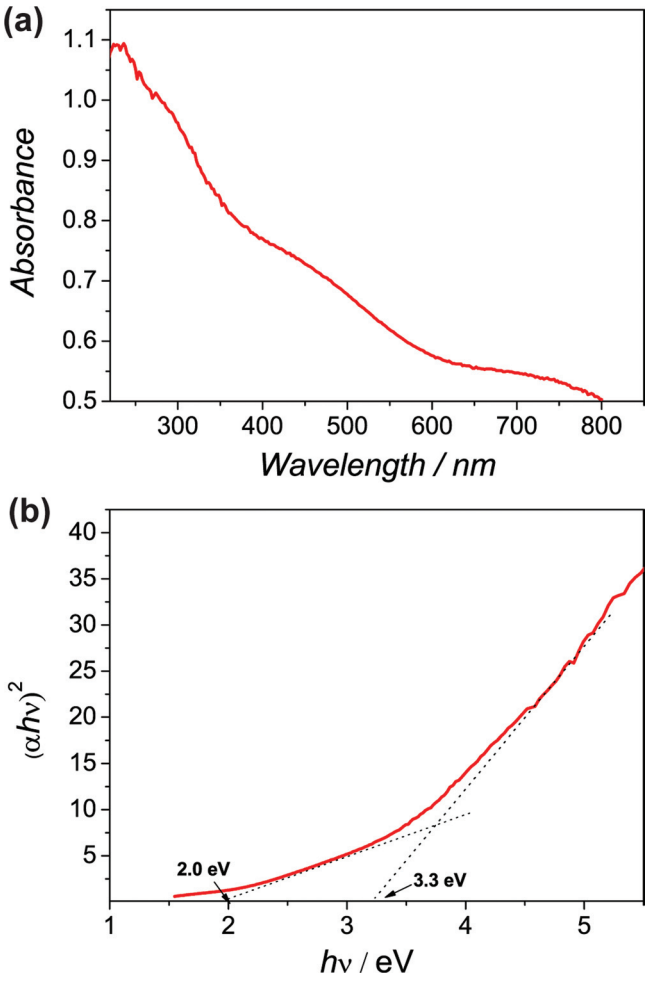

Figure 3. a) UV–vis adsorption spectrum of $NiCo_2O_4$ nanoplate. b) Optical band gap energy of $NiCo_2O_4$ nanoplate obtained by extrapolation to $(\alpha h\nu)^2 = 0$.

can be described as follows: tetrahedral high spin Co^{2+} ($e_g^4t_{2g}^3$), octahedral low spin Co^{3+} (t_{2g}^6), and Ni^{3+}($t_{2g}^6e_g^1$). The band structure of $NiCo_2O_4$ can be defined by taking the O 2p obital as the valence band and the Ni 3d and Co 3d orbitals as the conduction band. Since the high level Co 3d-e_g orbital is partially filled, the excitation of electrons from the Co 3d-t_{2g} orbital to the Co 3d-e_g orbital is possible.[10] Therefore, the as-observed two band gap energies in present study can be ascribed to the co-existence of high-spin and low-spin states of Co^{3+} in the $NiCo_2O_4$ spinel. Such a result has also been reported on the previous $NiCo_2O_4$ core-ring structure.[10]

The direct current (dc) conductivity was then measured in an individual $NiCo_2O_4$ nanoplate-based nanodevice. First, the as-transformed $NiCo_2O_4$ nanoplates were dispersed in ethanol and then dropped on an oxidized Si wafer substrate with a 200-nm-thick SiO_2 layer. Cr/Au (10 nm/100 nm) electrodes were deposited on an individual $NiCo_2O_4$ nanoplate to form a metal-$NiCo_2O_4$ nanoplate-metal nanodevice (**Figure 4**a). As can be seen in Figure 4b, the Cr/Au electrode pair is successfully bridged by only one single $NiCo_2O_4$ nanoplate benefited by its large lateral size. The distance between the two metal electrodes is about 2 μm. The typical *I–V* curve of each individual $NiCo_2O_4$ nanoplate was measured at room temperature to study the electrical transport within the (111) plane of $NiCo_2O_4$ nanoplate. As shown in **Figure 5**a and b, the as-obtained *I–V* characteristic is symmetrical and behaves linearly for applied voltages less than 0.3 V. This can be explained by the ohmic mechanism of conductivity in the low electrical field. The corresponding atomic force microscopy (AFM) image indicates an average thickness of about 70 nm based on statistical examination of more than 20 platelets (**Figure 6**). Since the thickness of the nanoplate is more than 50 nm, the tunnel current can be ignored. The effective length and cross-section of the $NiCo_2O_4$ nanoplate are about 2×10^{-4} cm and 4000 nm × 70 nm, respectively. Accordingly, the conductivity value, ≈62 S cm^{-1}, can be deduced by ignoring the contact resistance. Such a value is much larger than that of polycrystalline $NiCo_2O_4$ (≈0.6 S cm^{-1} at 300 °C) in previous study,[28] indicating that the conductivity of $NiCo_2O_4$ can be significantly enhanced in single-crystal nanostructures without abundant grain boundaries. The $NiCo_2O_4$ nanoplates with high

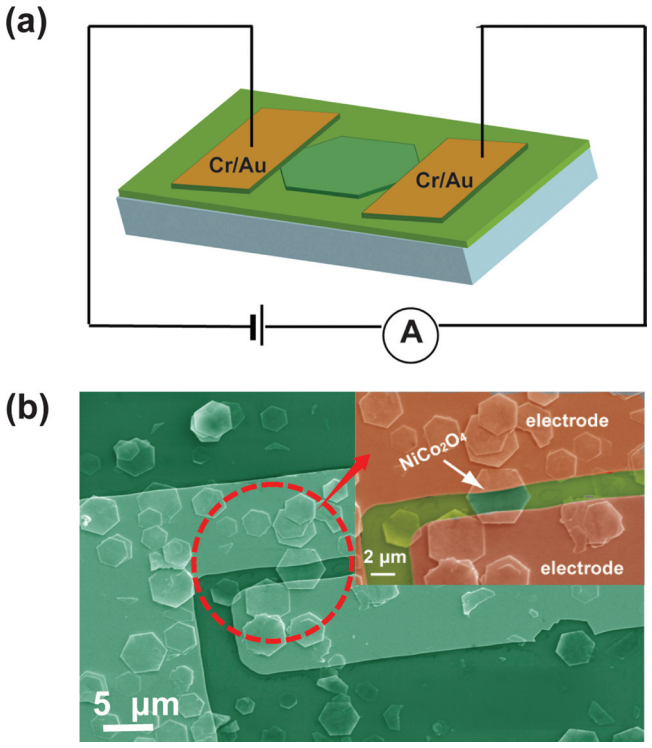

Figure 4. a) Schematic illustration of an individual $NiCo_2O_4$-nanoplate device. b) The corresponding SEM image of the device with a high-resolution image inserted.

conductivity may have potential applications on nanoelectrodes or nanosensors. The *I–V* curve increases exponentially as the applied voltage is further increased. To determine the dominant conduction mechanism, the logarithm of the current density (J) was plotted against the square root of the electric field ($E^{1/2}$) as shown in Figure 5c. One can see that the straight-line dependence of $E^{1/2}$ on J at an electric field higher than 59 V cm^{-1} (applied voltage: 0.3 V), suggesting Schottky emission. Generally, the Schottky current is expressed as follows:[29,30]

$$\ln J = \frac{\beta_{SE}}{kT}\sqrt{E} + \left[\ln(AT^2) - \frac{q\phi}{kT}\right] \quad (2)$$

Here, A is a constant, Φ is the Schottky barrier height, q is the electrical charge, k is Boltzmann's constant, and E is the electric field. The constant β_{SE} is given as follows:

$$\beta_{SE} = \sqrt{\frac{q^3}{4\pi\varepsilon_0\varepsilon_r}} \quad (3)$$

Here, ε_0 is the permittivity of the free space, and ε_r is the dielectric constant. The dielectric constant obtained from the slope is 11.9. The individual $NiCo_2O_4$ nanoplate here studied exhibited a combination of ohmic mechanism at a low applied voltage (<0.3 V) and Schottky emission at a high applied voltage (>0.3 V). This has also been observed in single $NH_4V_3O_8$ nanobelt and Sb_2S_3 nanowire devices described by other groups.[30,31]

The temperature dependence of electrical conductivity is a key characteristic of electric transport in any inorganic semiconductor system. In the present study, temperature dependent *I–V* measurements were taken at 10 K increments from a temperature of 8 to 300 K. As shown in **Figure 7**a, the current

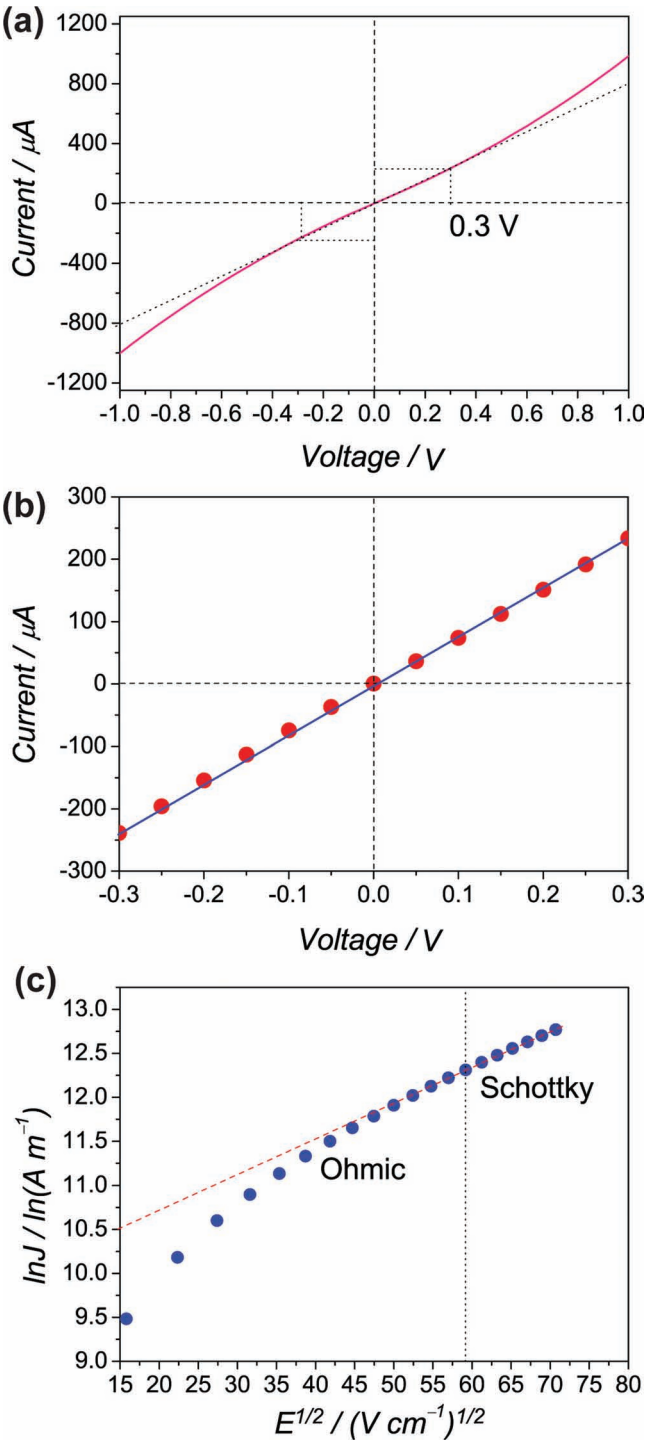

Figure 5. a) *I–V* curve recorded on an individual $NiCo_2O_4$ nanoplate at room temperature (300K). b) The enlarged part in (a) of applied voltage lower than 0.3 V. c) The experimental plot of $\ln(J)$ *vs* $E^{1/2}$ at the electric field between 15 and 71 V cm^{-1}. The red line illustrates a fitting curve to the law $\ln(J) \propto E^{1/2}$ at electric field intensity higher than 59 V cm^{-1}.

values of both the forward and reverse biases increased progressively with increasing temperature. The exponential decrease in resistance (R) versus temperature (T) (as shown in Figure 7b)

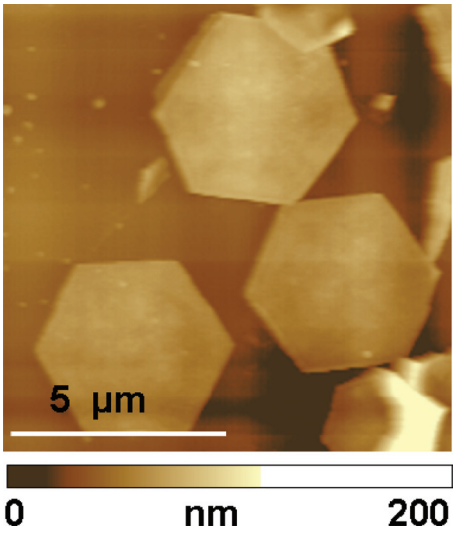

Figure 6. A typical AFM image of the as-transformed $NiCo_2O_4$ platelets dispersed on a Si substrate.

demonstrates typical semiconductor characteristics.[32] However, the conductivity σ cannot be fitted by the thermal excitation model given as $\sigma = \sigma_0 \exp(-\frac{\Delta E}{kT})$, where σ_0 is a constant and ΔE is the activation energy, excluding the simple thermal excitation mechanism for the increased conductivity as temperature increases. Then we consider hopping conduction models to fit the observed electrical properties. As proposed by Mott et al., two typical hopping mechanisms, called variable range hopping (VRH), which takes place at low temperatures, and nearest neighbor hopping (NNH), which takes place at high temperatures, are generally accepted from some semiconductor materials. The relationship between σ and T for the so-called VRH and NNH mechanisms can be expressed by the following equations:[33,34]

$$\sigma_1 = \sigma_0 \exp\left[-\left(\frac{T_0}{T}\right)\frac{1}{4}\right] \text{(VRH)} \quad (4)$$

$$\sigma_2 = \left[\frac{\upsilon_0 e^2 c(1-c)}{kTr}\right] \exp(-2\alpha r) \exp\left(\frac{-\Delta E}{kT}\right) \quad (5)$$

(NNH, T > θ_D, θ_D: Debye temperature)

Here, T_0 is the VRH characteristic temperature associated with the density of localized states at the Fermi energy, σ_0 is a constant, υ_0 is the longitudinal optical phonon frequency, α is the rate of wave-function decay, r is the average hopping distance, c is the fraction of sites occupied by electrons or polarons, and ΔE is the activation energy. In the present study, when the temperature was below 100K, the σ–T curve of our $NiCo_2O_4$ nanoplate could be well fit by the NNH model: $\sigma_1 = 102 \exp\left[-(\frac{720}{T})^{\frac{1}{4}}\right]$, with $\sigma_0 = 102$, $T_0 = 720$ (as shown in **Figure 8**a). When the temperature was higher than 100 K, the σ–T curve corresponded with the addition of the VRH and NNH models (Figure 8b): $\sigma = \sigma_2 + \sigma_1 = \frac{133252}{T} \exp\left(-\frac{0.066}{kT}\right) + 102 \exp\left[-\left(\frac{720}{T}\right)^{\frac{1}{4}}\right]$. The activation energy (ΔE) of the $NiCo_2O_4$ nanoplate was calculated to be 0.066 eV, which is a little larger than the value reported for $NiCo_2O_4$ bulk (0.03 eV).[35] The fitting results demonstrate that the NNH model dominates electrical transport at low

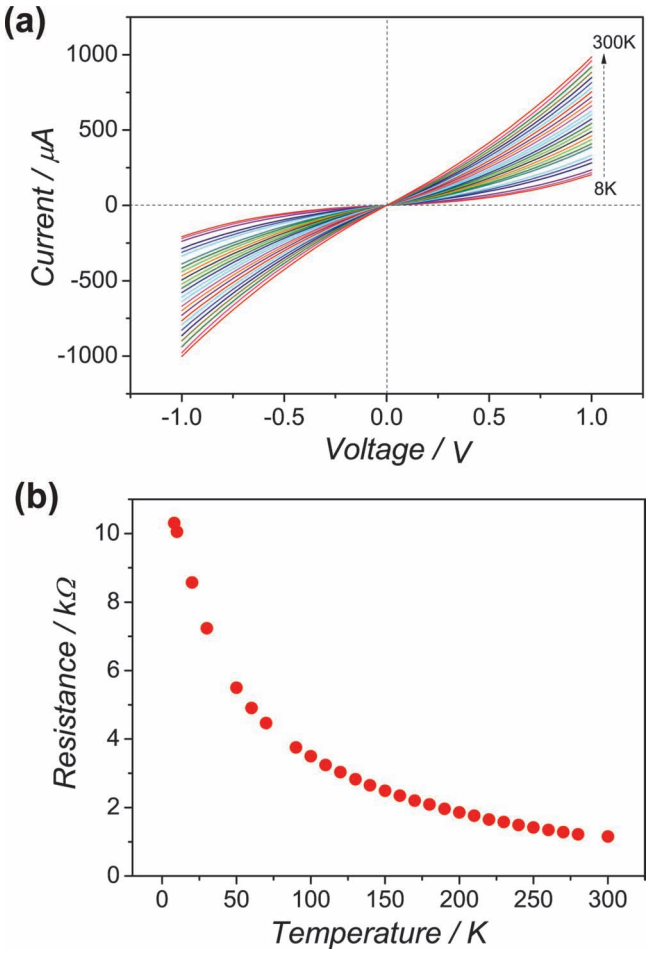

Figure 7. a) *I*–*V* curves of the individual $NiCo_2O_4$ nanoplate device recorded within the temperature range of 8–300 K. b) Temperature dependence of the resistance (*R*) as a function of temperature (*T*).

temperatures. As the temperature increases, both the NNH and VRH mechanisms contribute to transport of the carrier at a critical temperature of 100 K (Debye temperature). The hopping conduction suggests the presence of some surface defects or vacancies in our $NiCo_2O_4$ platelet despite of its single-crystal nature.

According to previous studies, both NiO and Co_3O_4 are intrinsic *p*-type semiconductors. However, it is still not clear whether *p*-type conductivity is maintained or if some transition to *n*-type conductivity occurs in $NiCo_2O_4$ spinels.[36,37] Because the exact conduction type of $NiCo_2O_4$ is still ambiguous,[38] the present study developed a preliminary understanding as follows: In Mott's mechanism, the conductivity of a semiconductor takes place as the carriers hop inside the material, and this electron hopping is assisted by atomic displacement in the lattice (phonons).[35] First, for the VRH model, a hopping step does not necessarily take place between nearest-neighbor hopping-sites, but may span a greater distance. The as-observed VRH conduction mechanism at $T < 100$ K may be explained by the fact that the optical phonons do not have enough energy to assist hopping as the temperature decreases.[20] Therefore, conductivity of the $NiCo_2O_4$ platelet at low temperatures is determined by the

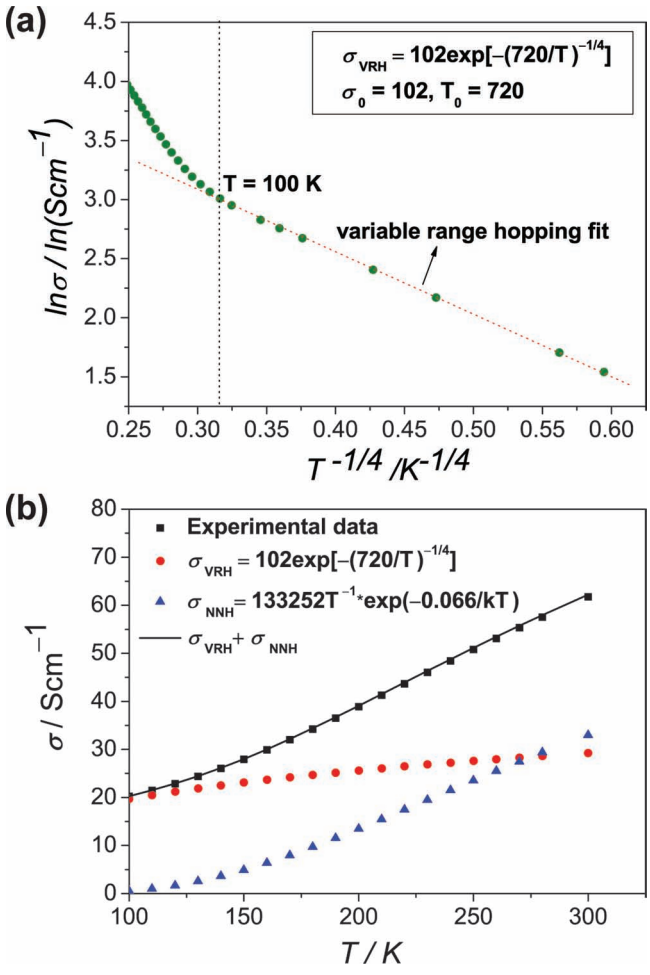

Figure 8. a) A plot of ln σ as a function of $T^{-1/4}$ (the red dashed line is the fit to the NRH model when $T < 100$ K). b) A black plot of σ (experimental data) as a function of T when $T > 100$ K. The red and blue plots represent the fitting results of the VRH and NNH models, respectively. The solid line is the best fits with the addition of the VRH and NNH models.

acoustic single-phonon-assisted hopping process, according to Schnakenberg's theory.[39] Second, as the temperature increases, NNH-mechanism electrical transport gradually become prominent. For the NNH model, the conduction process is considered in terms of optical-phonon-assisted hopping of small polarons between localized sites. Small polarons, for our $NiCo_2O_4$ platelet, can be regarded as the holes or electrons that are localized around the lattice sites. Because the localized carriers polarize the lattice around themselves, the coherent motion of free charge carriers through the lattice is destroyed, and the carriers must hop between localized states.[40] The hopping process inside the $NiCo_2O_4$ spinel nanoplate is schematically illustrated in **Figure 9**. We expect that these initial results will be useful to understanding the fundamental characteristics of $NiCo_2O_4$ and to designing functional nanodevices from both individual $NiCo_2O_4$ nanostructure and $NiCo_2O_4$ polycrystalline film. For the $NiCo_2O_4$ film consisted of numerous $NiCo_2O_4$ nanostructures, the conduction mechanism contains the hopping conduction inside individual $NiCo_2O_4$ nanostructure and

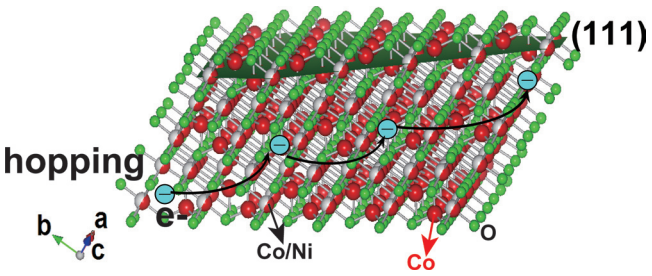

Figure 9. Schematic illustration of the hopping process in $NiCo_2O_4$ spinel nanoplate.

the hoping process between the grain boundariers due to the existence of junction barriers, which is consistent with the Schottky contact observed in the $NiCo_2O_4$ nanofilm-based photodetectors reported in our previous study.[13]

3. Conclusions

In conclusion, high-quality micrometer-sized $NiCo_2O_4$ nanoplates have been successfully prepared by a quasi-topotactic transformation from the hydroxide precursor, and the first electrical transport study of $NiCo_2O_4$ was performed based on an individual-$NiCo_2O_4$-nanoplate-device. A study of this nanoplate's temperature-dependent dc conductivity revealed exponential behavior, which shows the semiconductive nature of the $NiCo_2O_4$ nanoplate. The mechanisms of electrical conduction at low temperatures ($T < 100$ K) can be explained in terms of Mott's variable range hopping model. At high temperatures ($T > 100$ K), the electrical transport properties of the $NiCo_2O_4$ nanoplate contribute through both the variable range hopping and nearest neighbor hopping mechanism. Further investigation of the in-plane electrical transport properties along different directions inside the (111) top-surface of a hexagonal $NiCo_2O_4$ nanoplate through an electron-beam lithography technique is under way.

4. Experimental Section

Synthesis of $NiCo_2O_4$ Platelets: The $NiCo_2O_4$ platelets were prepared from their corresponding CoNi-LDH (layered double hydroxide) precursor $(Ni_{1/3}Co_{2/3}(OH)_2Br_{1/3}\cdot nH_2O)$. First, CoNi-LDH was synthesized by homogeneous precipitation as described previously.[25] Typically, 5 mmol of cobalt chloride ($CoCl_2\cdot 6H_2O$), 2.5 mmol of nickel chloride ($NiCl_2\cdot 6H_2O$) and 45 mmol of hexamethylenetetramine (HMT) were dissolved in 1000 cm^3 of deionized water. The $CoCl_2$-$NiCl_2$-HMT solution was refluxed for 5 h under continuous magnetic stirring and nitrogen protection. The light-pink precipitate (Brucite phase) was recovered by filtration, washed with deionized water and anhydrous ethanol in turn, and finally air-dried at room temperature. Then, 2 mmol (0.186 g) of the light-pink Brucite phase were dispersed in 100 cm^3 of acetonitrile containing 6.67 mmol of bromine. The mixture was sealed in an airtight capped flask and magnetically stirred for 24 h. The yellow-green product, identified as bromide intercalated CoNi-LDH, was collected by centrifugation and washed with copious amounts of anhydrous ethanol to remove the excess bromine adsorbed on the powder.[25] Second, $NiCo_2O_4$ platelets were obtained by the thermal transformation of the CoNi-LDH precursor at 500 °C for 1 h with a heating rate of 1 °C min^{-1}.

Device Construction: The as-transformed $NiCo_2O_4$ nanoplates were dispersed in ethanol and then dropped on an oxidized Si wafer substrate with a 200-nm SiO_2 top layer. Au/Cr electrodes were deposited on an individual $NiCo_2O_4$ nanoplate through a photolithography, electron-beam deposition, and lift-off process. The current–voltage (I–V) characteristics of the device were recorded at room (HiSOL, Inc) and low temperatures (Nagase Electronic Equipment Service Co.) probing systems and a semiconductor parameter analyzer (Keithley 4200 Instruments, Inc).

Characterization: The synthesized $NiCo_2O_4$ samples were characterized using a transmission electron microscope (TEM, JEOL 2010). Tapping-mode AFM images of the $NiCo_2O_4$ nanoplates were obtained using a Shimadzu Instruments SPM-9500J3 system. UV-vis absorption spectra were recorded using a Hitachi U-4100 spectrophotometer.

Acknowledgements

This work was supported by the National Natural Science Foundation of China (Grant Nos. 91123006, 51133001, 21001028, 51002032 and 21074023), Shanghai Science and Technology Foundation (10JC1401900), the Innovative Team of Ministry of Education of China (IRT0911), the National Basic Research Program of China (Grant No. 2012CB932303), Shanghai Chenguang Foundation (11CG06), Shanghai Pujiang Program (11PJ1400300), and the Programs for Professor of Special Appointment (Eastern Scholar) at Shanghai Institutions of Higher Learning and for New Century Excellent Talents in University (NCET). We thank Professor Hongjun Xiang from Department of Physics, Fudan University for valuable discussion on the mechanisms of electrical conduction.

Received: September 11, 2011
Published online: January 19, 2012

[1] J. Xiang, J. W. Lu, Y. Hu, H. Yan, C. M. Lieber, *Nature* **2006**, *441*, 489.
[2] X. S. Fang, T. Y. Zhai, U. K. Gautam, L. Li, L. M. Wu, Y. Bando, D. Golberg, *Prog. Mater. Sci.* **2011**, *56*, 175.
[3] X. Wu, Z. Chen, G. Q. Lu, L. Z. Wang, *Adv. Funct. Mater.* **2011**, *21*, 4167.
[4] X. Chen, Z. Guo, W. H. Xu, H. B. Yao, M. Q. Li, J. H. Liu, X. J. Huang, S. H. Yu, *Adv. Funct. Mater.* **2011**, *21*, 2049.
[5] Y. Cui, X. F. Duan, J. T. Hu, C. M. Lieber, *J. Phys. Chem. B* **2000**, *104*, 5213.
[6] M. Tambe, S. Ren, S. Gradečak, *Nano Lett.* **2010**, *10*, 4584.
[7] B. K. Sarker, S. Shekhar, S. I. Khondaker, *ACS Nano* **2009**, *3*, 478.
[8] J. F. Marco, J. R. Gancedo, M. Gracia, J. L. Gautier, E. I. Ríos, H. M. Palmer, C. Greaves, F. J. Berry, *J. Mater. Chem.* **2001**, *11*, 3087.
[9] B. Cui, H. Lin, J.-B. Li, X. Li, J. Yang, J. Tao, *Adv. Funct. Mater.* **2008**, *18*, 1440.
[10] B. Cui, H. Lin, Y. Z. Liu, J. B. Li, P. Sun, X. C. Zhao, C. J. Liu, *J. Phys. Chem. C* **2009**, *113*, 14083.
[11] S. Verma, H. M. Joshi, T. Jagadale, A. Chawla, R. Chandra, S. Ogale, *J. Phys. Chem. C* **2008**, *112*, 15106.
[12] R. Alcántara, M. Jaraba, P. Lavela, J. L. Tirado, *Chem. Mater.* **2002**, *14*, 2847.
[13] L. F. Hu, L. M. Wu, M. Y. Liao, X. S. Fang, *Adv. Mater.* **2011**, *23*, 1988.
[14] L. Li, X. S. Fang, T. Y. Zhai, M. Y. Liao, U. K. Gautam, X. C. Wu, Y. Koide, Y. Bando, D. Golberg, *Adv. Mater.* **2010**, *22*, 4151.
[15] J. Joo, B. Y. Chow, J. M. Jacobson, *Nano Lett.* **2006**, *6*, 2021.
[16] B. Paul, K. H. Andrew, A. C. Aqif, O. Lucy, T. Benedicte, B. Peter, A. D. Jawwad, *Ind. Eng. Chem. Res.* **2007**, *46*, 4830.
[17] Z. Liu, R. Ma, M. Osada, N. Iyi, Y. Ebina, K. Takada, K. T. Sasaki, *J. Am. Chem. Soc.* **2006**, *128*, 4872.
[18] R. Ma, Z. Liu, K. Takada, N. Iyi, Y. Bando, T. Sasaki, *J. Am. Chem. Soc.* **2007**, *129*, 5257.
[19] Y. Kobayoshi, X. Ke, H. Hata, P. Schiffer, T. E. Mallouk, *Chem. Mater.* **2008**, *20*, 2374.
[20] J. Park, E. Lee, Y. W. Lee, C. E. Lee, *Appl. Phys. Lett.* **2006**, *89*, 183114.
[21] J. F. Liu, Q. H. Li, T. H. Wang, D. P. Yu, Y. D. Li, *Angew. Chem. Int. Ed.* **2004**, *43*, 5048.
[22] Y. Li, L. An, C. Lu, J. Liu, *Nano Lett.* **2006**, *6*, 148.
[23] L. Li, Y. Zhang, X. S. Fang, T. Y. Zhai, M. Y. Liao, X. L. Sun, Y. Koide, Y. Bando, D. Golberg, *J. Mater. Chem.* **2011**, *21*, 6525.
[24] B. Hu, L. Q. Mai, W. Chen, F. Yang, *ACS Nano* **2009**, *3*, 478.
[25] J. Liang, R. Ma, N. Iyi, Y. Ebina, K. Takada, T. Sasaki, *Chem. Mater.* **2010**, *22*, 371.
[26] L. F. Hu, R. Ma, T. C. Ozawa, T. Sasaki, *Angew. Chem. Int. Ed.* **2009**, *48*, 3846.
[27] L. F. Hu, R. Ma, T. C. Ozawa, T. Sasaki, *Inorg. Chem.* **2010**, *49*, 2960.
[28] Y. Fujishiro, K. Hamamoto, O. Shino, S. Katayama, M. Awano, *J. Mater. Sci.* **2004**, *15*, 769.
[29] S. Chakraborty, M. K. Bera, G. K. Dalapati, D. Paramanik, S. Varma, P. K. Bose, S.Bhattacharya, C. K. Maiti, *Semicond. Sci. Technol.* **2006**, *21*, 467.
[30] L. Q. Mai, C. S. Lao, B. Hu, J. Zhou, Y. Y. Qi, W. Chen, E. D. Gu, Z. L. Wang, *J. Phys. Chem. B* **2006**, *110*, 18138.
[31] H. Bao, X. Cui, C. M. Li, Q. Song, Z. Lu, J. Guo, *J. Phys. Chem. C* **2007**, *111*, 17131.
[32] R. S. Vemuri, K. K. Bharathi, S. K. Gullapalli, C. V. Ramana, *ACS Appl. Mater. Interfaces* **2010**, *2*, 2623.
[33] N. F. Mott, *Philos. Mag.* **1969**, *19*, 835.
[34] N. F. Mott, E. A. Davis, *Electronic Process in Non-Crystalline Materials*, Clarendon Press, UK **1979**.
[35] N. J. Tharayil, S. Sagar, R. Raveendran, A. V. Vaidyan, *Physica B* **2007**, *399*, 1.
[36] C. F. Windisch Jr., K. F. Ferris, G. J. Exarhos, S. K. Sharma, *Thin Solid Films*, **2001**, *398*, 45.
[37] C. F. Windisch Jr., K. F. Ferris, G. J. Exarhos, S. K. Sharma, *J. Vac. Sc. Technol.* **2001**, *19*, 1647.
[38] It is still difficult to completely clarify the conduction type of $NiCo_2O_4$. Previous study variously described as *p* type or semimetallic-to-metallic suggesting *n* type.[34] Our experiment based on a field-effect transistor (FET) device from an individual $NiCo_2O_4$ platelet also failed to illuminate the conduction mechanism (not shown here).
[39] J. Schnakenberg, *Phys. Status Solidi* **1968**, *28*, 623.
[40] C. F. Windisch Jr., K. F. Ferris, G. J. Exarhos, S. K. Sharma, *Thin Solid Films* **2002**, *420*, 89.